

Article

Effect of Sintering Temperature on Phase Formation and Mechanical Properties of Al–Cu–Li Alloy Prepared from Secondary Aluminum Powders

Antonio Cañadilla ^{1,†}, Juan Pablo Sanhueza ², Cristóbal Montalba ^{3,*,†} and Elisa María Ruiz-Navas ⁴

¹ E.T.S. Ingeniería Industrial, Institute of Energy Research and Industrial Applications, Universidad de Castilla-La Mancha (UCLM), 13071 Ciudad Real, Spain; antonio.canadilla@uclm.es

² Departamento de Ingeniería de Materiales, Universidad de Concepción, Edmundo Larenas 315, 4070415 Concepción, Chile; juanpasanhueza@udec.cl

³ Departamento de Tecnologías Industriales, Facultad de Ingeniería, Universidad de Talca, Camino a los Niches km 1, 3340000 Curicó, Chile

⁴ Departamento de Física, Universidad Carlos III de Madrid, Avda. Universidad 30, 28911 Leganés, Spain; emruiz@ing.uc3m.es

* Correspondence: cmontalba@utalca.cl

† These authors contributed equally to this work.

Abstract: Aluminum and its alloys are very versatile materials used in a wide range of applications due to the initial characteristics of pure aluminum and the combination of properties obtained from its blend with other elements. Considering that aluminum is the second-most-produced metal after steel, and that its production will increase over time based on the demand to produce products through conventional and additive methodologies, this will lead to an increase in the energy consumed as well as the footprint of carbon generated. It is for this reason that the generation of competitive aluminum alloys must be approached from secondary sources (recycling). To address these environmental issues, in this work, 2070 aluminum alloy (AA2070) samples were manufactured using secondary aluminum powder and compared with the primary aluminum source. The samples were compacted at 700 MPa and sintered at a different range of temperatures between 525 °C and 575 °C. The study includes thermodynamic modeling, microstructure, and mechanical characterization. Microstructure and phases characterization were carried out via scanning electron microscopy (SEM) and X-ray diffraction (XRD) analysis, respectively, whereas the mechanical characterization comprised relative density evaluation, hardness, and flexion tests. Results were compared with the calculation of phase stability using Thermo-Calc software 2020a. Based on the results obtained, it can be concluded that the secondary AA2070 optimal sintered temperature, where the components raised the highest mechanical properties and effective relative density range, is 575 °C. Furthermore, the recycled alloys have similar relative densities and flexural strengths than the corresponding alloys made from primary aluminum powder.

Keywords: secondary aluminum alloy; AA2070; powder metallurgy; Thermo-Calc; mechanical properties



Citation: Cañadilla, A.; Sanhueza, J.P.; Montalba, C.; Ruiz-Navas, E.M. Effect of Sintering Temperature on Phase Formation and Mechanical Properties of Al–Cu–Li Alloy Prepared from Secondary Aluminum Powders. *Metals* **2024**, *14*, 12. <https://doi.org/10.3390/met14010012>

Academic Editor: Jürgen Eckert

Received: 11 October 2023

Revised: 12 November 2023

Accepted: 16 November 2023

Published: 21 December 2023



Copyright: © 2023 by the authors. Licensee MDPI, Basel, Switzerland. This article is an open access article distributed under the terms and conditions of the Creative Commons Attribution (CC BY) license (<https://creativecommons.org/licenses/by/4.0/>).

1. Introduction

Aluminum, the second-most-produced metal globally, faces environmental concerns due to its anticipated quadrupling demand by 2025 [1,2]. Primary aluminum production from bauxite requires ten times more energy than secondary processing. Recycling aluminum scrap emerges as a sustainable alternative, offering up to 95% energy and emission savings, coupled with an 85% reduction in manufacturing costs [3,4].

Given the environmental impact of primary production and the high recyclability of aluminum, addressing primary aluminum recycling becomes crucial. Various proposed routes for recycling aluminum chips and powders exist [5–9]. A circular economy for aluminum scraps in powder form, especially through powder metallurgy, shows promise,

particularly in the growing additive manufacturing market. Valued at around USD12.6 billion in 2020 [10], the additive manufacturing industry requires more input materials and innovative production methods to meet aluminum feedstock needs, emphasizing sustainability and a circular economy [11–13].

Forming alloys from recycled sources aims not only to cut costs, but also to enhance the value of secondary metals by exercising control over alloy composition during secondary aluminum production. To compete with primary aluminum alloys and other light alloys and composites, achieving superior performance and lower costs is essential [1,14].

The most extensively studied families of aluminum alloys are the 2XXX and 7XXX families [15–18]. Among these, the Al–Cu–Li alloys (2XXX series), specifically those of the third generation, stand out for their high performance and elevated costs [19,20]. Introduced in the 1980s, the third-generation Al–Li alloys, characterized by copper as the primary alloying element and lithium content ranging between 1 and 2 wt.%, offer numerous advantages over 2XXX and 7XXX aluminum alloys. These advantages include a reduced density, an increased fracture toughness, good fatigue resistance, and an improved corrosion resistance [21,22]. Considering the context of reducing environmental impact and cost without lowering the value of the alloy, Al–Cu–Li alloys appear to be a critical component for research and improvement, considering the use of secondary aluminum powders.

Aluminum Alloy 2070 (AA2070) is a recent addition to the third generation of Al–Li alloys, designed as a silver-free alternative to the AA2050 alloy with the aim of reducing costs and enhancing specific strength and damage tolerance [23,24]. Limited studies currently exist on the microstructural characterization, process parameterization, or property modification of AA2070 alloy, whether primary or secondary. Semenov et al. [25] explored corrosion resistance against various aggressive atmospheres, Liu et al. [26] investigated the impact of plastic deformation and the addition of small Sc percentages on AA2070 microstructure and mechanical properties, and Staroselsky [27] assessed potential applications of these alloys in the aeronautic and aerospace sectors.

Given the notable advantages of Al–Li–Cu family alloys, this study aims to investigate the utilization of secondary aluminum powders in designing and producing a secondary AA2070 aluminum alloy, comparing it with the same alloy derived from a primary source.

To understand the thermal behavior of primary and secondary AA2070 alloy, a theoretical study of the alloy was carried out using Thermo-Calc to analyze the phases formed at different sintering temperatures. The first are those associated with the typical harmful elements of secondary aluminum (Fe and Si), as well as those that can improve the sintering process and are related to the cracking of the aluminum oxide layer. Elemental powders from different sources followed the same processing route, i.e., the adjustment of the chemical composition, the formation of samples through pressing and sintering, and characterization. For each temperature, the theoretical and experimental phases formation as well as their physical, microstructural, and mechanical properties were studied.

2. Materials and Experimental Procedures

2.1. Raw Materials

2.1.1. Primary Aluminum

The base metal used for the primary alloy was commercially pure aluminum (Al) manufactured by Alfa Aesar (Haverhill, MA, USA). According to the specifications provided by the company, it has a purity of 99.5% and an average particle size of 44 μm (Figure 1).

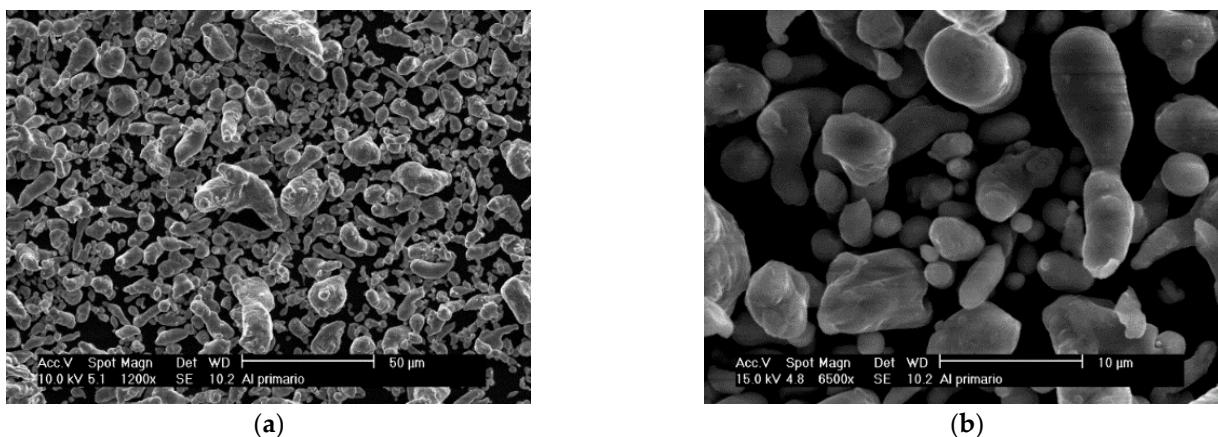


Figure 1. Primary Al powder microscopy: (a) $\times 1200$, (b) $\times 6500$.

2.1.2. Secondary Aluminum

The base metal used to generate secondary aluminum alloys was obtained from recycling aluminum alloys of the 1XXX series. Figure 2 presents an average size and irregular shape of the aluminum powders obtained after the respective recovery process, that is, chip and bulk secondary aluminum melting and subsequent atomization.

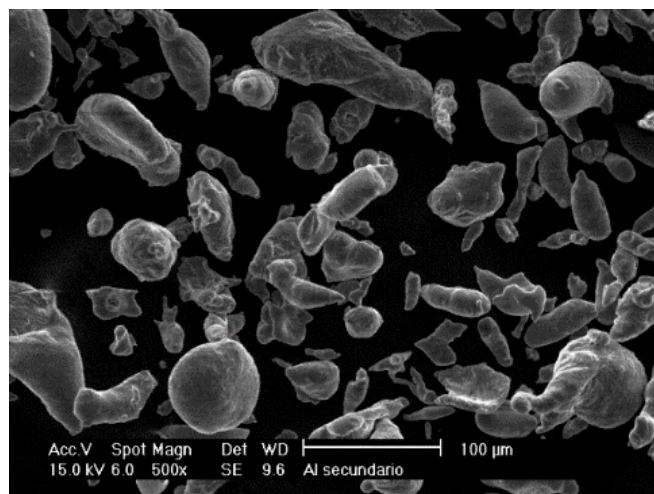


Figure 2. Scanning electron microscopy of recycled aluminum powder $\times 500$.

The chemical composition of the recycled aluminum powder is shown in Table 1. Low amounts of oxygen were evidenced (values were not highlighted in the mentioned table). Figure 3 shows the particle size distribution with $d_{50} = 39 \mu\text{m}$ obtained from a laser particle size distribution analysis carried out with a Mastersizer Malvern Instruments S.L. (Indian Trail, NC, USA). The density of the alloy has been defined by the producer and corresponds to 2701 g/cm^3 .

Table 1. Composition of recycled aluminum powder.

Secondary Aluminum Composition (wt.%)					
Al	Si	Fe	Mg	Cu	Others
98.61	0.32	0.38	0.35	0.08	0.34

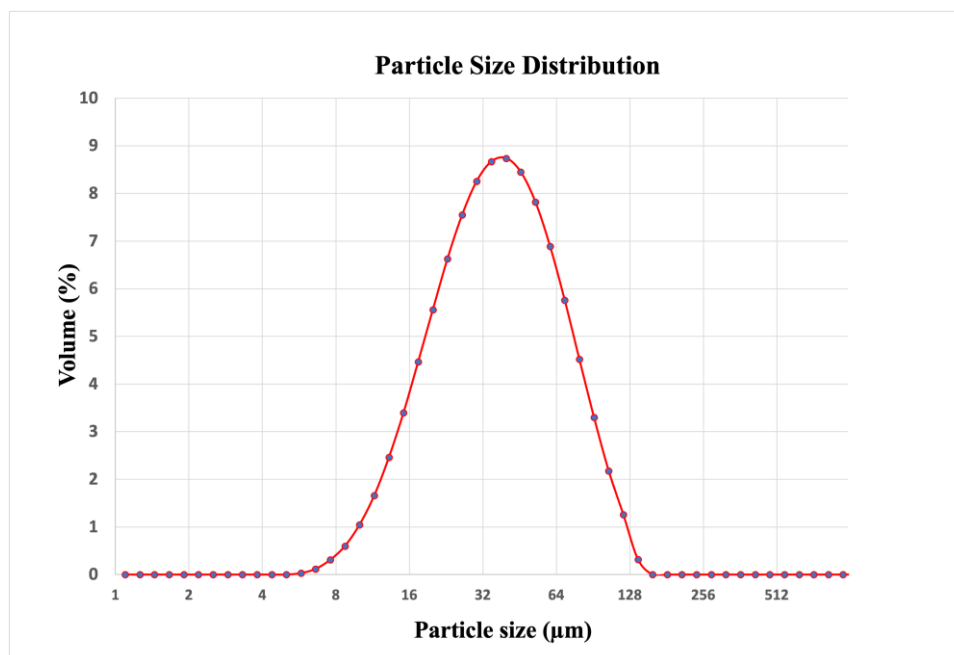


Figure 3. Particle size distribution of recycled aluminum powder.

2.2. Design and Manufacturing of the Alloy

Considering the stoichiometric composition of the AA2070 alloy defined by The Aluminum Association Inc. (Arlington, DC, USA), the alloys studied were developed by combining elemental powders of each component from primary pure aluminum and secondary aluminum. The chemical compositions are shown in Table 1. Alloy elements added to achieve the ranges established for the AA2070 alloy were the following: 50 μm copper, purity 99.5%; 50 μm magnesium, purity 99.8%; 60 μm lithium, purity 99.5%; 40 μm zinc, purity 99%; 45 μm manganese, purity 99.5%; and 40 μm titanium, purity 99.9%. In the alloy formed from secondary aluminum, the magnesium was adjusted, and the Fe and Si values (typical elements of secondary aluminum alloys) were maintained. The chemical composition of the designed alloys is presented in Table 2.

Table 2. Composition of primary and secondary AA2070 alloys manufactured in the present work.

Weight %	Cu	Li	Mg	Si	Fe	Zn	Mn	Ti	Al
Chemical Composition Range for AA2070	2.9–3.8	1.0–1.4	0.05–0.4	0.12	0.15	0.1–0.5	0.1–0.5	0.1	Bal.
Average Chemical Composition Primary AA2070	3.28	1.17	0.25	0.04	0.07	0.28	0.34	0.12	Bal.
Average Chemical Composition Secondary AA2070	3.45	1.20	0.42	0.31	0.36	0.35	0.37	0.14	Bal.

The elements involved in the alloy were weighed stoichiometrically with reference to the average weight of the range established by The Aluminum Association Inc. The powders were meticulously blended using a mechanical mixer, specifically a Turbula powder mixer for 45 min. To ensure thorough homogenization, 304 L steel balls were incorporated to avoid powder agglomeration. Furthermore, we implemented intermediate sieving steps to remove any agglomerates, and to enhance the homogeneity of the powder mixture before compaction.

The powders were compacted in a uniaxial press manufactured by Microtest (Altopascio, Italy), applying a pressure of 700 MPa and obtaining cylindrical specimens of 16 mm in

diameter and 2 mm in height for microstructural and phase tests, as well as rectangular specimens of $30 \times 12 \times 6 \text{ mm}^3$ for mechanical bending tests.

Considering that the transient liquid phase phenomenon is critical for a successful sintering (penetration of the surface oxides) [28,29], as well as the conservation of the stoichiometry of the alloy (lithium content), three sintering temperatures were considered in the study: 525 °C, 550 °C, and 575 °C. The criterion of selected temperatures was to examine sintering in solid-state at (525 °C) and liquid-assisted modes (550 °C and 575 °C). Sintering was performed in a *Carbolite S302RR* tubular furnace with a high-purity N_2 atmosphere, considering a heating ramp of 5 °C/min and a 60 min sintering plateau. Cooling was performed inside the furnace.

2.3. Characterization of Samples

The relative density of the samples was calculated using the Archimedes method according to the ASTM B311-17 standard [30]. The microstructure of the sintered samples was analyzed via scanning electron microscopy (SEM) in a JEOL JSM-6610LV (Leeds, UK) equipped with an EDAX DX-4 (Madrid, Spain) energy-dispersive X-ray spectroscopy (EDS) analyzer. The phases of each sample were analyzed via X-ray diffraction using the PHILIPS PW3040/000 equipment (Tokyo, Japan) working at a voltage of 40 kV and an intensity of 40 mA. The mechanical properties of the samples were measured using the Vickers hardness test, measured using HMV Micro Hardness Tester (Shimadzu, Kyoto, Japan) and bending tests according to the UNE-EN ISO 3325 standard [31] using a Microtest EM2/FT (Madrid, Spain) universal testing machine with a 15 kN load cell.

3. Results and Discussion

3.1. Thermodynamic Modeling Using Thermo-Calc

The theoretical study of the AA2070 alloy phases was carried out using the Thermo-Calc software version 2020a based on the compositions presented in Table 2.

Considering the data presented above, the theoretical phase diagram simulation of the recycled AA2070 alloy was performed using Thermo-Calc, as shown in Figure 4. The diagram has been constructed as a function of the weight percentage of iron in the alloy due to its potential influence on the sintering processing and detrimental phase formation, impacting on the alloy behavior, specifically on the microstructure and mechanical properties of the final material. In contrast, the other alloy elements remain at fixed values established by previous studies [32].

In order to identify the stable phases at the different sintering temperatures in the diagram, a dashed line was used to show the percentage of iron that characterizes the secondary AA2070 alloy, approximately 0.35 wt.%, and three black dots on it to indicate the three sintering temperatures studied (525 °C, 550 °C, and 575 °C). The presence of iron was a relevant variable to consider since it has practically no solubility in aluminum in the solid state (~0.05 wt.%). This tends to form intermetallic secondary phases combined with other elements, severely impairing the properties of the compound.

All this allows for identifying the phases that would theoretically be found in the alloy microstructure based on the sintering temperature, after equilibrium cooling, and their chemical composition (at.%) and total mass fraction. The theoretical study is relevant because constituents and phases formed during heat treatment not only affect the behavior of the final product, but also predict the sintering process through the formation of the liquid phase. Table 3 shows the phases that are thermodynamically stable at 525 °C, and Table 4 shows the equivalents for sintering at 550 °C and 575 °C (approximately the same).

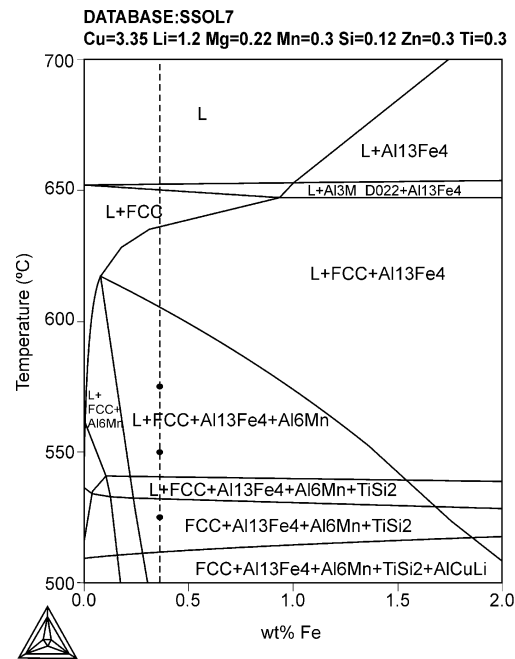


Figure 4. Phase diagram of AA2070 alloy obtained with Thermo-Calc. Sintering temperatures are indicated by black dots.

Table 3. Chemical composition (at.%) and mass fraction of the stable phases at 525 °C calculated using Thermo-Calc for the secondary AA2070 alloy.

PHASES	Al	Li	Cu	Mg	Mn	Fe	Si	Zn	Ti	Mass Fraction
	at.%									
Al ₁₃ Fe ₄	60.97	-	-	-	4.30	34.66	-	-	-	0.008
Al ₆ Mn	74.50	-	-	-	11.98	13.52	-	-	-	0.015
FCC_A2	94.54	1.23	3.43	0.23	0.08	0.008	0.09	0.3	0.08	0.976
TiSi ₂	-	-	-	-	-	-	53.98	-	46.02	0.0006

Table 4. Chemical composition (at.%) and mass fraction of the stable phases at 550 °C and 575 °C calculated using Thermo-Calc for the secondary AA2070 alloy.

PHASES	Al	Li	Cu	Mg	Mn	Fe	Si	Zn	Ti	Mass Fraction
	at.%									
Liquid	77.38	2.04	24.22	0.78	0.03	0.03	1.52	0.61	0.003	0.032
Al ₁₃ Fe ₄	60.96	-	-	-	4.51	34.53	-	-	-	0.011
Al ₆ Mn	74.50	-	-	-	12.18	13.32	-	-	-	0.010
FCC_A2	95.25	1.20	0.027	2.72	0.13	0.01	0.08	0.296	1.06	0.946

Considering these theoretical results, it is convenient to analyze the evolution of the stable phases that form the microstructure of the alloy based on the sintering temperature.

In the samples sintered at 525 °C, the stable theoretical phases, according to the Thermo-Calc results, are the primary solid phase FCC_A2, which corresponds to a solid solution rich in aluminum, and the secondary phases Al₁₃Fe₄, Al₆Mn, and TiSi₂ (although the latter in almost imperceptible quantities). On the other hand, the stable phases at sintering temperatures of 550 °C and 575 °C are the liquid phase FCC_A2, and the secondary phases Al₆Mn and Al₁₃Fe₄. As the sintering temperature increases, the phase in the liquid

state acquires greater importance, so that it changes from being null in the case of the process at 525 °C to exceeding 3% for the temperatures of 550 °C and 575 °C. This fact has a significant influence on sintering. This is a process that occurs entirely in the solid state in the first case, and in the liquid phase in the second, and as a direct result, this can seriously affect the final properties of the material [29].

Regardless of the sintering temperature, the most important solid-state phases are aluminum with an FCC crystalline structure and the secondary phases $Al_{13}Fe_4$ and Al_6Mn . Both secondary phases have the highest iron content, much higher in $Al_{13}Fe_4$ (≈ 35 at.%), but it is also relevant in the case of Al_6Mn (≈ 15 at.%) due to the importance of the mass fraction that this phase represents on the total. The two secondary phases are maintained with a percentage by weight of around 1% regardless of the temperature (within the ranges considered in this study, from 525 °C to 575 °C).

The remaining phase mentioned in the attached table ($TiSi_2$) is not within the scope of this work because it has the smallest percentage and therefore has little effect on the alloy. However, it is worth mentioning that the minimum amount of this phase at 525 °C disappears entirely in temperatures above 550 °C.

3.2. Calculation of Relative Density Using the Archimedes Method

Table 5 shows the results obtained for both primary and secondary AA2070 alloys. Theoretical density used to measure the relative density was 2.64 g/cm^3 [33].

Table 5. Relative density of the sintered samples of the AA2070 alloy.

AA2070 Alloy	Temperature (°Celsius)	Average Density (g/cm^3)	Average ρ_{relative} (%)	Average Porosity (%)
Primary	525	2.52	95.90 ± 0.25	4.10
	550	2.52	95.81 ± 0.24	4.19
	575	2.47	93.85 ± 0.33	6.15
Secondary	525	2.49	94.84 ± 0.27	5.16
	550	2.49	94.61 ± 0.44	5.39
	575	2.49	94.68 ± 0.18	5.32

Density results reveal discernible distinctions between alloys derived from primary and secondary sources, with the latter exhibiting diminished values relative to the former. The influential role of iron in the densification processes of aluminum alloys is notably underscored. In the broader context, primary aluminum alloys consistently manifest a superior relative density in contrast to their secondary counterparts. This phenomenon is ascribed to intrinsic attributes inherent in primary alloys, encompassing the initial powder's purity and the absence of impurities inherent in recycled materials. These factors collectively contribute to a heightened compactness and density within the resultant microstructure.

However, a noteworthy decline in relative density becomes apparent in samples sintered at 575 °C, reaching an average value even below that of secondary AA2070 alloys at the corresponding temperature. The impact of iron on the densification of sintered aluminum alloys has been systematically documented in antecedent studies [34]. Importantly, the absence of iron in this investigation significantly influences the sintering dynamics of the Al–Cu–Li primary alloy at 575 °C.

The examination of the relevant literature underscores an optimal intermediate sintering temperature of approximately 550 °C for 2XXX family alloys containing lithium [35]. Beyond this temperature, an expansion in the volume of the liquid phase is anticipated, leading to a heightened porosity in the primary sample at 575 °C (this assertion can be substantiated through the results in Table 4 by employing Thermo-Calc). The reactivity of lithium at elevated temperatures, resulting in the generation of pores and the loss of the element, introduces variations in density, alongside documented grain growth and a reduction in mechanical strength [36]. Qi et al.'s study [37] suggests that aluminum–

lithium alloys fabricated through powder metallurgy necessitate post-treatment, such as hot extrusion, to enhance density. This is attributed to the intrinsic nature of aluminum and the reactivity of impurities. Rodríguez-González et al. [38], in a study on a similar alloy (AA2060), identified a liquid phase at temperatures of 550 °C and 575 °C (with varying proportions) using Thermo-Calc. However, subsequent hot-processing revealed disparate behaviors, characterized by volumetric stability at 550 °C and the emergence of discontinuities at 575 °C. This underscores the sensitivity of aluminum–lithium alloys to slight variations in the formation of the liquid phase, attributable to the low melting point of lithium. Interestingly, the presumed reactive effect of lithium on the reduction in physical properties (and mechanical properties in Section 3.5) is not observed in the behavior of secondary AA2070 alloy samples, where density remains constant across the entire temperature range.

The elucidation of this behavior may be found in Shaffer et al.'s research [34], which emphasizes the impact of iron on liquid film migration (LFM). Iron impedes the mobility of copper in the matrix, leading to its accumulation at the grain boundary and the creation of copper-rich phases in those regions (corroborated by microstructural studies). This adversely affects the sintering process, resulting in diminished densification for secondary alloys. However, it also indicates that in the primary alloy without iron content, a different phenomenon occurs during the formation of the liquid phase. This is marked by a heightened mobility at the grain boundaries, fostering an increase in porosity. Additionally, it is postulated that larger grain sizes may be generated in the primary alloy at higher sintering temperatures compared to the secondary alloy, where the presence of iron induces “grain boundary pinning” effects. Furthermore, the study conducted by Zhang et al. [39], examining the interaction of Al–Li alloy powders with iron, suggests that iron may exert a stabilizing effect on lithium reactivity. This allows the secondary alloy to remain more stable against the formation of the liquid phase and subsequent loss, as observed in the primary AA2070 alloy.

While the density evaluation data for primary and secondary alloys suggest an optimal sintering temperature of 550 °C, such a conclusion necessitates the consideration of other results, particularly those pertaining to mechanical properties. A comprehensive evaluation of all findings is imperative to derive a nuanced and conclusive determination of the most suitable sintering temperature for the Al–Cu–Li alloy.

3.3. Microstructural Analysis of Sintered Components

The microstructural analysis using scanning electron microscopy (SEM) aimed to compare the microstructures of primary and secondary alloys at each sintering temperature.

In Figure 5, the microstructures of primary and secondary AA2070 alloys sintered at 525 °C are presented. The images confirm the successful compaction and sintering processes, resulting in components with appropriate densification more notorious for primary than secondary alloys. However, some residual microporosity is observed, likely due to the insufficient sintering temperature of 525 °C, which was not enough to generate a liquid phase during the process. This limitation hinders achieving better results compared to higher temperatures [40,41]. In both microstructures, a continuous phase acting as the matrix (FCC_A2 phase described theoretically by Thermo-Calc) can be visibly distinguished, along with a secondary phase in the form of coarse particles, whose composition will be detailed later. Notably, at this sintering temperature, the primary material (Figure 5a) exhibits fewer coarse secondary phases (brighter, associated with a higher molecular weight than the matrix) compared to the recycled material (Figure 5b).

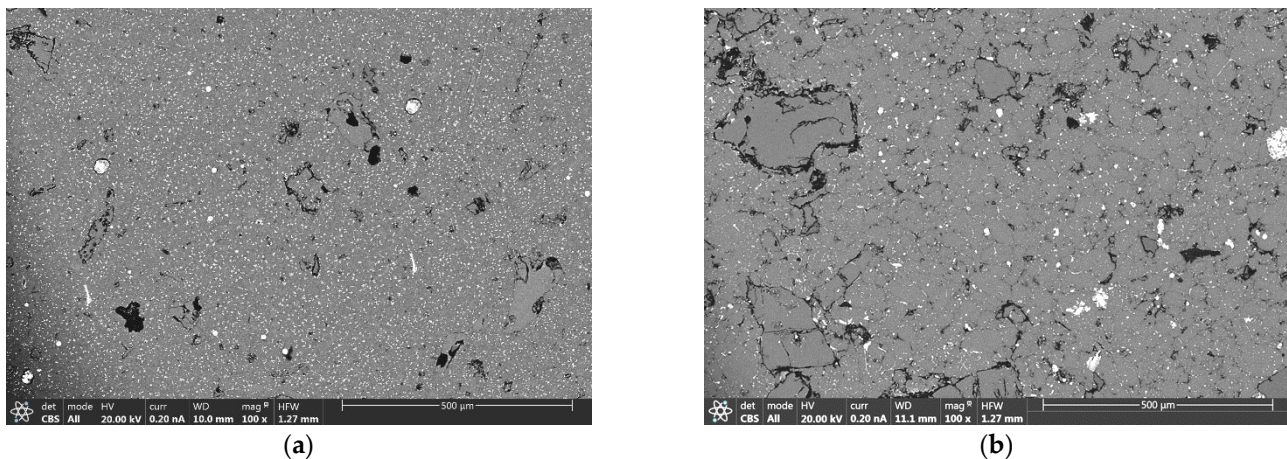


Figure 5. SEM image of AA2070 alloy after sintering at 525 °C: (a) primary aluminum alloy and (b) secondary aluminum alloy.

As the sintering temperature is increased to 550 °C (Figure 6), the microporosity in both primary and secondary alloys decrease significantly. The porosity becomes very limited, isolated, and lacks interconnections, well within the standardized limits for this type of material. This increase in densification is expected to positively impact the final mechanical properties. In both materials, the FCC_A2 phase remains the dominant continuous phase in the microstructure. It is noteworthy that despite the elevated sintering temperature, the secondary phase remains stable and exhibits similar percentages in both the primary material (Figure 6a) and recycled material (Figure 6b). However, the morphology of the particles differs, with a finer and more uniform distribution in the material obtained from primary aluminum.

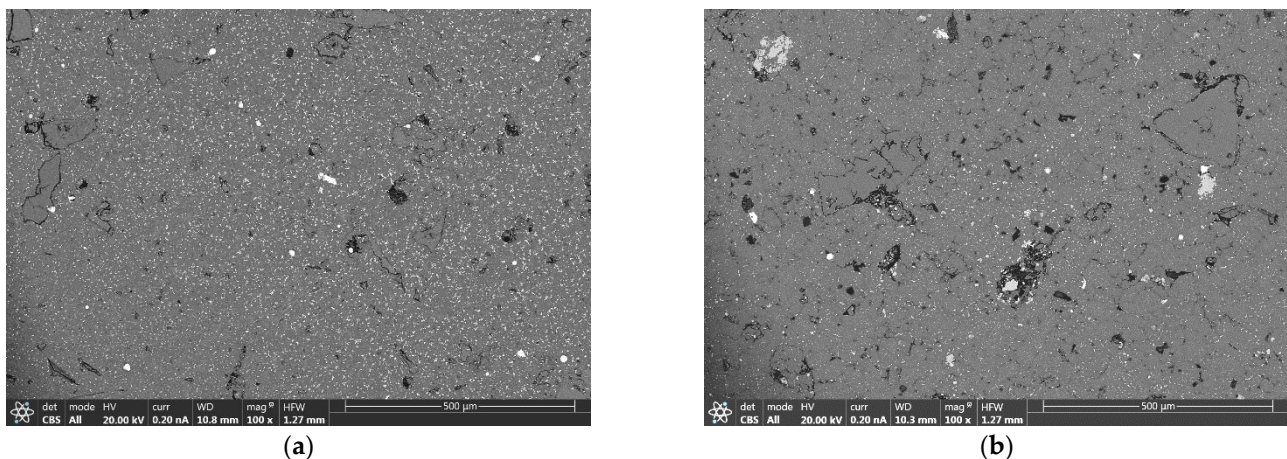


Figure 6. SEM image of AA2070 alloy after sintering at 550 °C: (a) primary aluminum alloy and (b) secondary aluminum alloy.

Finally, the samples synthesized at 575 °C (Figure 7), for the case of the primary samples (Figure 7a), do not show significant variation in porosity and phase distribution compared to the previous sample, but there is an increase in grain size. In the case of the secondary sample (Figure 7b), a decrease in porosity is observed, as well as a reduction in the size of secondary phases, accompanied by a more homogeneous distribution compared to those observed at lower temperatures. However, the elimination of the secondary phase is not definitive in either case.

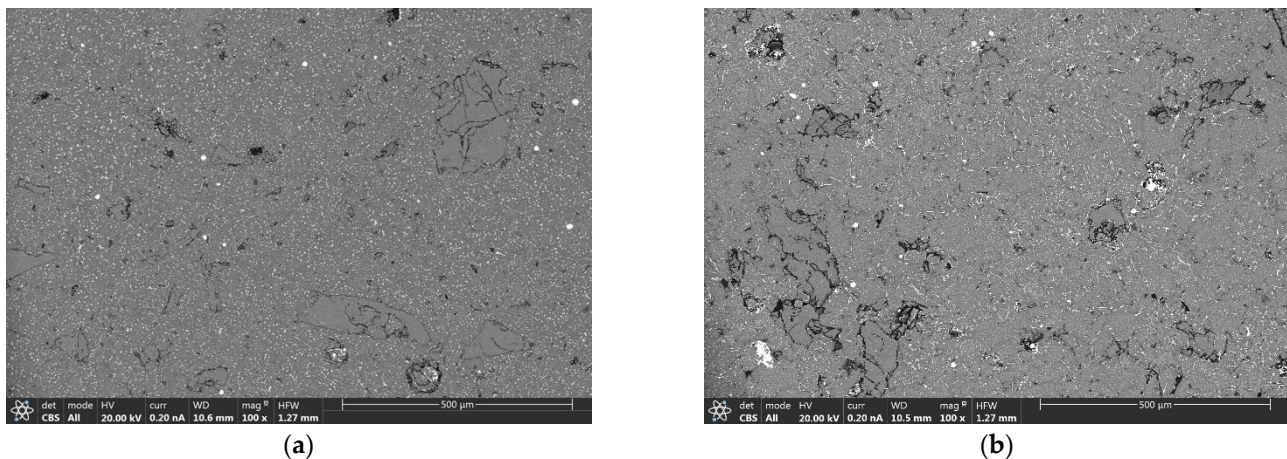


Figure 7. SEM image of AA2070 alloy after sintering at 575 °C: (a) primary aluminum alloy and (b) secondary aluminum alloy.

From the metallographic images obtained for different sintering temperatures of primary and secondary aluminum alloys, we can observe the aluminum-based matrix and a distinct bright appearance phase typical of Al–Cu–X, which presumably arises from the dissolution of copper during transient liquid phase. At temperatures of 525 °C and 550 °C, there is a noticeable difference in the distribution of the phase associated with copper. Additionally, there is a difference in terms of quantity and distribution, with the secondary alloy exhibiting a lower quantity of the phase that is more agglomerated compared to the primary alloy, where the phase appears in a fine and homogeneously distributed manner. This phenomenon aligns with the findings from the study by Schaffer et al. [34], where it was explained that iron delays the migration of the liquid phase due to copper reduction caused by the presence of iron. The secondary aluminum sample sintered at 575 °C shows an increase in the distribution of the phase due to the higher temperature, but the trend remains consistent with lower temperatures.

EDX analysis was conducted for each alloy at different sintering temperatures to identify the alloying elements and the composition of the different phases. Although the information is provided in a semi-quantitative manner, the analysis allows us to determine the alloying elements and existing phases, aligning with the theoretical results obtained from Thermo-Calc. Table 6 displays the results obtained for the matrix phase of the secondary AA2070 alloy at the three sintering temperatures, while Table 7 presents the analysis on the secondary phase particles uniformly distributed in the microstructure for the three sintered samples. Both tables provide results from various measurements taken at equivalent points along the microstructure, and the figure shows one of these points. Notably, the percentages of lithium will not be considered in the following tables since they cannot be detected via EDX analysis.

Table 6. EDX measurement of the composition of the main FCC_A2 phase of the AA2070 alloy recycled after sintering.

Element (at.%)	Sintering Temperature		
	525 °C	550 °C	575 °C
Al	96.6	98.3	98.7
Cu	3.4	1.7	1.3

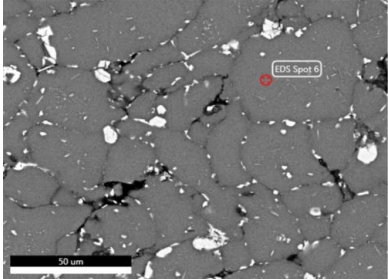
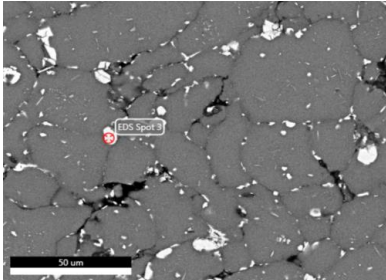


Table 7. EDX measurement of the composition of the secondary phase particles of recycled AA2070 alloy after sintering.

Element (at.%)	Sintering Temperature		
	525 °C	550 °C	575 °C
Al	78.5	77.4	76.0
Cu	16.6	3.0	3.5
Mn	-	1.7	1.8
Fe	4.9	12.3	13.2
Si	-	5.6	5.5



Considering the values provided in the table, the FCC_A2 solid phase corresponds to an aluminum-rich solid solution [42] with a low percentage of copper, which aligns with the theoretical predictions from Thermo-Calc. The atomic percentage of copper (Cu) in this phase is consistent with the percentage determined by the theoretical model discussed in the previous section. Notably, it is observed that the solubility of copper in the aluminum solution modifies as the sintering temperature rises, leading to a decrease in copper content from approximately 3.5 to 1.30 at.% when transitioning from 525 °C to 575 °C.

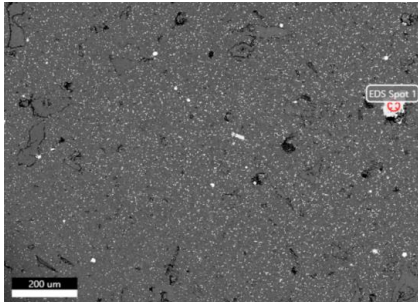
This trend can be demonstrated through the graphs presented in Figure 4 and their corresponding compositions, which illustrate that the diffusivity of copper increases with higher sintering temperatures, resulting in a greater presence of copper in the liquid phase. Consequently, this phenomenon significantly impacts the reduction in sample porosity and enhances sample densification at elevated temperatures. The increased diffusion of copper contributes to the formation of a more homogeneous microstructure, leading to improved properties in the final material.

Regarding the secondary phase of the alloy treated at 575 °C, its atomic composition (76% Al, 3.5% Cu, 1.8% Mn, 13.2% Fe, 5.5% Si) bears a striking resemblance to the Al₆Mn phase predicted by the Thermo-Calc study, despite being values obtained through a semi-quantitative analysis. The stability of this phase across the different sintering temperatures tested explains why it does not undergo complete dilution in the AA2070 alloy. Moreover, it aligns with the specifications of stable precipitates commonly formed in this type of alloy, which have been the subject of numerous studies [43]. The presence of Al₆Mn, and possibly the Al₁₃Fe₄ phase (not observed in the analysis), is likely associated with the higher iron content originating from impurities in the recycled aluminum powder, representing up to 15 at.% of the total composition.

For comparison, Table 8 presents the composition of the secondary phase detected in the AA2070 primary alloy components sintered at 525 °C.

Table 8. EDX measurement of the composition of the secondary phase particles of the primary AA2070 alloy after sintering.

Element (at.%)	Sintering Temperature
	525 °C
Al	62.8
Mn	23.0
Cu	14.2



The analysis reveals that the secondary phase of the primary alloy is primarily composed of aluminum and manganese, with no presence of iron and silicon impurities. Consequently, it can be concluded that the inclusion of iron impurities in the recycled aluminum powder leads to alterations in the microstructure of the sintered material, particularly in relation to the secondary phase. Given the significant percentage of iron in the recycled material, it is expected that this aspect will have an impact on the mechanical properties, as detailed in the subsequent section.

3.4. X-ray Diffraction Analysis

In addition to the analysis conducted using electron microscopy and energy-dispersive X-ray fluorescence, consolidated samples from both primary and secondary aluminum were subjected to X-ray diffraction (XRD) analysis to complement and confirm the findings. The X-ray diffraction patterns obtained from the primary and secondary samples of the AA2070 alloy are found to be identical. Consequently, this XRD analysis serves to confirm the dominant presence of high-volume fraction phases, namely the FCC_A2 matrix, and the Al_2Cu equilibrium precipitate. Figure 8 displays the diffraction pattern corresponding solely to the secondary AA2070 alloy.

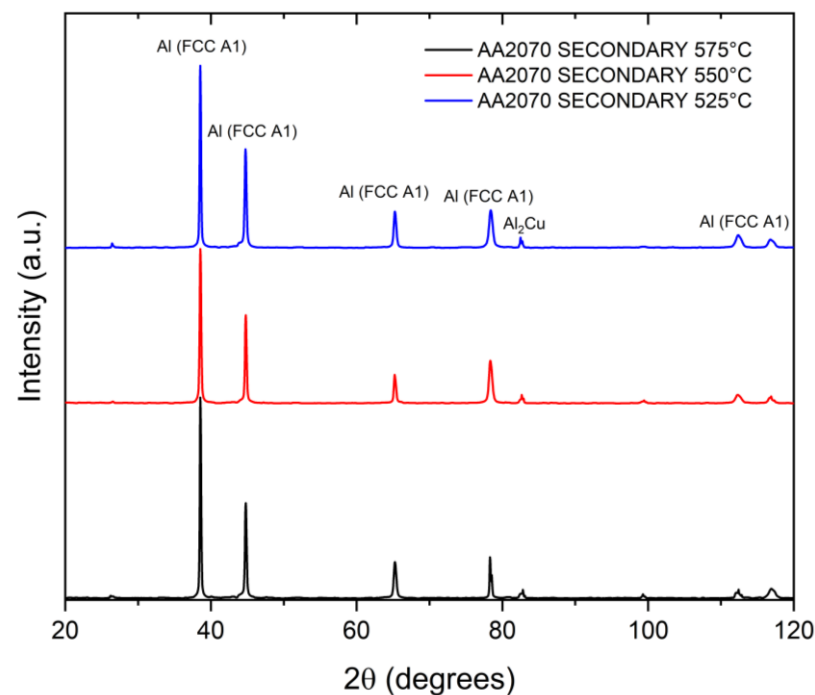


Figure 8. Diffraction pattern of AA2070 alloy with secondary aluminum.

3.5. Mechanical Characterization

To determine the mechanical behavior of the different alloys, Vickers hardness tests and flexural tests were conducted on both primary and secondary samples for each sintering temperature.

In Figure 9, the variation in hardness for the primary and secondary AA2070 alloys can be observed. Regarding primary alloys, there is a tendency to maintain a relatively constant hardness with a slight decrease at temperatures above 550 °C.

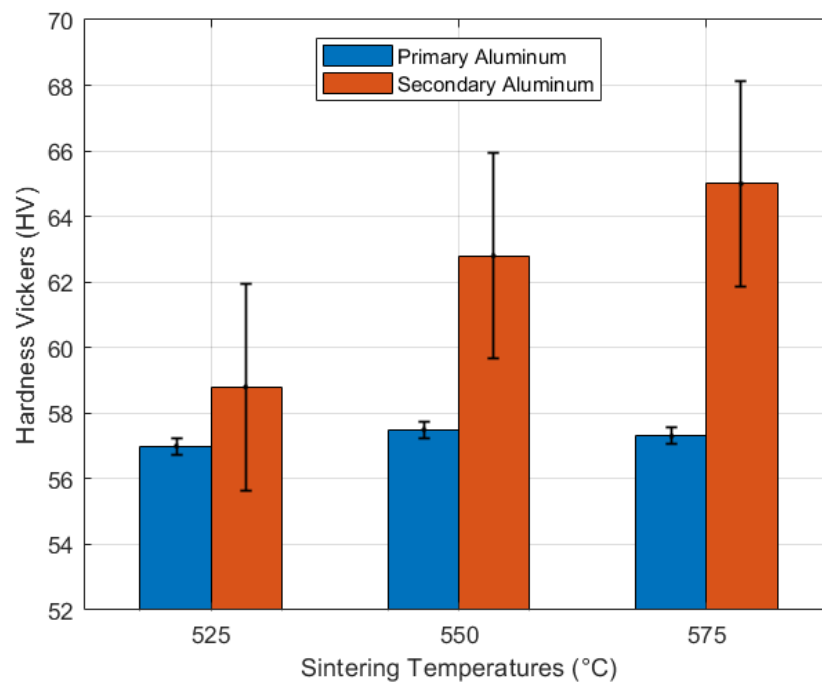


Figure 9. Hardness Vickers for primary and secondary AA2070.

Regarding secondary alloys, the hardness values are higher than those of the primary alloys for each temperature, and their hardness increases with rising sintering temperature. This behavior can be explained by the formation of a secondary iron-based phase, $\text{Al}_{13}\text{Fe}_4$, which was determined through Thermo-Calc simulation and confirmed via EDS in the microstructural study. Numerous studies have established that the generation of iron-based secondary phases, regardless of their stoichiometry, enhances the stiffness of aluminum alloys [40,41]. Additional results not included in this study allowed for the calculation and determination that the iron-based secondary phases in the secondary alloys reached hardness values of approximately 140 HV. The hardness results highlight the dispersion of results in the secondary alloys, attributed to the presence of dispersed Al_xFe_y secondary phases in the samples.

Figure 10 presents the values of bending properties associated with both primary and secondary AA2070 alloys.

The results of the bending tests, as represented by the transverse rupture strength, exhibit a significant difference behavior for primary and secondary alloys. At 525 °C, the difference is 113.3 MPa, decreasing to 67.61 MPa at 550 °C, and then nearly leveling off at the maximum temperature between the primary and secondary alloy (approximately 5.48 MPa). The primary alloy shows a slight decrease in strength as the sintering temperature increases, while conversely, the secondary alloy AA2070 exhibits an upward trend, with a less pronounced increase between temperatures of 525 °C and 550 °C (approximately 20.58 MPa) and a more pronounced increase between temperatures of 550 °C and 575 °C (approximately 57.52 MPa).

It is crucial to note that these behaviors cannot be solely attributed to the effects of iron, as mentioned in the case of hardness results [44,45]. In bending tests, other factors influencing transverse rupture strength, such as ductility and toughness, must be considered. In such tests, the toughness and a material's ability to absorb energy before fracturing are fundamental, forming the basis for understanding the behavior of both primary and secondary alloys [46].

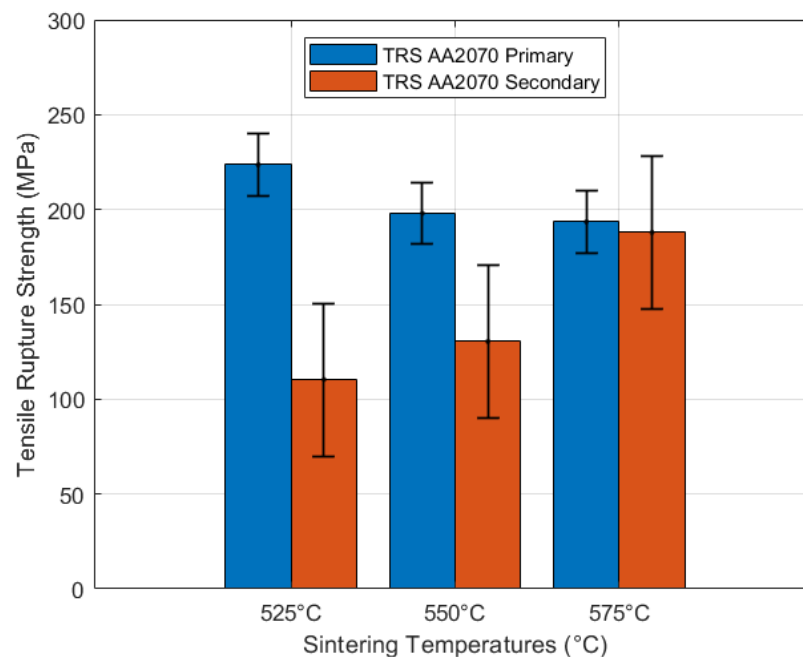


Figure 10. TRS results of primary and secondary AA2070.

The behavior of primary alloys under bending loads tends to decrease as the temperature rises. This is primarily due to an increase in grain size with higher sintering temperatures, making them less resistant. Furthermore, at elevated temperatures, there is a higher likelihood of the formation of a liquid phase, weakening the grain boundaries [47].

In contrast, lower temperatures can result in smaller grain sizes, contributing to increased toughness and deformation capacity before fracture. It is likely that, at temperatures exceeding 525 °C, aluminum–copper–lithium alloys develop a microstructure with a larger grain size, a more uniform phase distribution, and better matrix cohesion [47].

Furthermore, differences in phase distribution in secondary alloys may explain their improved performance in bending at higher temperatures. In bending tests, local concentrations of harder or more brittle phases act as crack initiation points, weakening the sample and reducing its transverse rupture strength, particularly at lower temperatures. However, at higher temperatures, particle coalescence in the green bodies is more effective due to increased thermal energy, facilitating particle movement and coalescence [34,38,47]. This results in a more homogeneous phase distribution in the microstructure, explaining the differences in mechanical properties between secondary alloys at low and high temperatures [34,47]. At lower temperatures, coalescence may be less effective, allowing differences in phase distribution to be more pronounced. This can be visually observed in Figures 5b and 6b, where secondary alloys exhibit a more heterogeneous phase distribution, comparable to the secondary sample sintered at 575 °C (Figure 7b).

4. Conclusions

The primary objective of this study was to formulate a high-performance Al–Li–Cu alloy, specifically AA2070, using secondary raw materials and employing the powder metallurgy route. A comparison was made between the primary production process and that which was generated from secondary sources.

Our findings indicate the feasibility of synthesizing high-performance aluminum alloys, in this case, AA2070, from secondary material sources. The resulting alloys exhibited consolidated properties that closely resembled primary alloys.

Regarding density, the results obtained through the Archimedes method revealed that at sintering temperatures of 525 °C and 550 °C, the primary alloy exhibited a higher density compared to the secondary alloy. However, at 575 °C, the density of the primary

alloy decreased below the average of secondary alloys across the entire range of evaluated temperatures. This phenomenon was attributed to the influence of iron content, which inhibits the formation of the liquid phase, thereby allowing for greater diffusive stability at high temperatures.

A microstructural analysis of primary and secondary alloys showed the formation of phases to be consistent with what was predicted by the thermal simulation performed using Thermo-Calc. As the sintering temperature increased, secondary alloys achieved greater homogeneity in the distribution of secondary phases, similar to primary alloys. However, grain growth was observed in primary alloys, which was not observed in secondary alloys due to grain boundary pinning.

Regarding mechanical properties, it was found that secondary alloys exhibited higher hardness compared to primary alloys, primarily due to the presence of iron-based intermetallic phases, which impart high hardness to the matrix. Bending test results indicated a better performance of primary alloys at low temperatures. However, as the sintering temperature increased, primary alloys tended to decrease their bending capacity due to increased grain size and the formation of the liquid phase at 575 °C. In contrast, secondary alloys exhibited a trend of increased bending capacity, reaching results similar (but still lower) to primary alloys at 575 °C. This phenomenon is attributed to a more uniform distribution of secondary phases (intermetallic) in the matrix, which enhances coalescence with the matrix and reduces stress concentration points.

In summary, this study has demonstrated the feasibility of synthesizing high-performance aluminum alloys from secondary sources using powder metallurgy. Secondary alloys exhibited properties comparable to primary alloys, suggesting significant potential for their application in various industrial applications. The results also highlight the influence of iron content on density and property stability at high temperatures, which may be of great relevance in future developments of high-performance secondary aluminum alloys.

Author Contributions: Conceptualization, C.M.; Methodology, A.C., C.M. and E.M.R.-N.; Software, J.P.S.; Validation, E.M.R.-N.; Investigation, C.M. and E.M.R.-N.; Resources, C.M.; Writing—original draft, A.C. and C.M.; Writing—review and editing, J.P.S.; Supervision, E.M.R.-N.; Funding acquisition, C.M. All authors have read and agreed to the published version of the manuscript.

Funding: This study was supported by ANID through the project FONDECYT Initiation No. 11201232.

Data Availability Statement: The data presented in this study are available on request from the corresponding author. The data are not publicly available due to privacy concerns.

Acknowledgments: The corresponding author disclosed receipt of the following financial support for the research and publication of this article: In addition, the authors would like to thank Banco Santander for the financing granted through the Santander Mobility Grant for Young Researchers 2019.

Conflicts of Interest: The authors declare no conflict of interest.

References

1. Gautam, M.; Pandey, B.; Agrawal, M. *Chapter 8—Carbon Footprint of Aluminum Production: Emissions and Mitigation*; Muthu, S.S., Ed.; Butterworth-Heinemann: Boston, UK, 2018; pp. 197–228. [[CrossRef](#)]
2. Pedneault, J.; Majeau-Bettez, G.; Krey, V.; Margni, M. What future for primary aluminium production in a decarbonizing economy? *Glob. Environ. Chang.* **2021**, *69*, 102316. [[CrossRef](#)]
3. Brough, D.; Jouhara, H. The aluminium industry: A review on state-of-the-art technologies, environmental impacts and possibilities for waste heat recovery. *Int. J. Thermofluids* **2020**, *1–2*, 100007. [[CrossRef](#)]
4. Haraldsson, J.; Johansson, M.T. Review of measures for improved energy efficiency in production-related processes in the aluminium industry—From electrolysis to recycling. *Renew. Sustain. Energy Rev.* **2018**, *93*, 525–548. [[CrossRef](#)]
5. Wan, B.; Chen, W.; Lu, T.; Liu, F.; Jiang, Z.; Mao, M. Review of solid state recycling of aluminum chips. *Resour. Conserv. Recycl.* **2017**, *125*, 37–47. [[CrossRef](#)]
6. Moghimian, P.; Poirié, T.; Habibnejad-Korayem, M.; Zavala, J.A.; Kroeger, J.; Marion, F.; Larouche, F. Metal powders in additive manufacturing: A review on reusability and recyclability of common titanium, nickel and aluminum alloys. *Addit. Manuf.* **2021**, *43*, 102017. [[CrossRef](#)]

7. Kadir, M.I.A.; Mustapa, M.S.; Latif, N.A.; Mahdi, A.S. Microstructural Analysis and Mechanical Properties of Direct Recycling Aluminium Chips AA6061/Al Powder Fabricated by Uniaxial Cold Compaction Technique. *Procedia Eng.* **2017**, *184*, 687–694. [[CrossRef](#)]
8. Fuziana, Y.F.; Warikh, A.R.M.; Lajis, M.A.; Azam, M.A.; Muhammad, N.S. Recycling aluminium (Al 6061) chip through powder metallurgy route. *Mater. Res. Innov.* **2014**, *18*, S6-354–S6-358. [[CrossRef](#)]
9. Pulido-Suárez, P.A.; Uñate-González, K.S.; Tirado-González, J.G.; Esguerra-Arce, A.; Esguerra-Arce, J. The evolution of the microstructure and properties of ageable Al-Si-Zn-Mg alloy during the recycling of milling chips through powder metallurgy. *J. Mater. Res. Technol.* **2020**, *9*, 11769–11777. [[CrossRef](#)]
10. Sandeep, B.; Kannan, T.T.M.; Chandradass, J.; Ganesan, M.; John Rajan, A. Scope of 3D printing in manufacturing industries—A review. *Mater. Today Proc.* **2021**, *45*, 6941–6945. [[CrossRef](#)]
11. Sauerwein, M.; Doubrovski, E.; Balkenende, R.; Bakker, C. Exploring the potential of additive manufacturing for product design in a circular economy. *J. Clean. Prod.* **2019**, *226*, 1138–1149. [[CrossRef](#)]
12. Raabe, D.; Ponge, D.; Uggowitz, P.J.; Roscher, M.; Paolantonio, M.; Liu, C.; Antrekowitsch, H.; Kozeschnik, E.; Seidmann, D.; Gault, B.; et al. Making sustainable aluminum by recycling scrap: The science of ‘dirty’ alloys. *Prog. Mater. Sci.* **2022**, *128*, 100947. [[CrossRef](#)]
13. Hettiarachchi, B.D.; Brandenburg, M.; Seuring, S. Connecting additive manufacturing to circular economy implementation strategies: Links, contingencies and causal loops. *Int. J. Prod. Econ.* **2022**, *246*, 108414. [[CrossRef](#)]
14. Stemper, L.; Tunes, M.A.; Tosone, R.; Uggowitz, P.J.; Pogatscher, S. On the potential of aluminum crossover alloys. *Prog. Mater. Sci.* **2022**, *124*, 100873. [[CrossRef](#)]
15. Li, S.; Yue, X.; Li, Q.; Peng, H.; Dong, B.; Liu, T.; Yang, H.; Fan, J.; Shu, S.; Qiu, F.; et al. Development and applications of aluminum alloys for aerospace industry. *J. Mater. Res. Technol.* **2023**, *27*, 944–983. [[CrossRef](#)]
16. Abd El-Aty, A.; Xu, Y.; Guo, X.; Zhang, S.-H.; Ma, Y.; Chen, D. Strengthening mechanisms, deformation behavior, and anisotropic mechanical properties of Al-Li alloys: A review. *J. Adv. Res.* **2018**, *10*, 49–67. [[CrossRef](#)]
17. Azarniya, A.; Taheri, A.K.; Taheri, K.K. Recent advances in ageing of 7xxx series aluminum alloys: A physical metallurgy perspective. *J. Alloys Compd.* **2019**, *781*, 945–983. [[CrossRef](#)]
18. Khalid, M.Y.; Umer, R.; Khan, K.A. Review of recent trends and developments in aluminium 7075 alloy and its metal matrix composites (MMCs) for aircraft applications. *Results Eng.* **2023**, *20*, 101372. [[CrossRef](#)]
19. Starke, E.A. Historical Development and Present Status of Aluminum–Lithium Alloys. In *Aluminum-Lithium Alloys: Processing, Properties, and Applications*; Elsevier: Amsterdam, The Netherlands, 2014; pp. 3–26. [[CrossRef](#)]
20. Dorin, T.; Vahid, A.; Lamb, J. Aluminium Lithium Alloys. In *Fundamentals of Aluminium Metallurgy: Recent Advances*; Elsevier: Amsterdam, The Netherlands, 2018; pp. 387–438. [[CrossRef](#)]
21. Dursun, T.; Soutis, C. Recent developments in advanced aircraft aluminium alloys. *Mater. Des.* **2014**, *56*, 862–871. [[CrossRef](#)]
22. Hajjioui, E.A.; Bouchaala, K.; Faqir, M.; Essadiqi, E. A review of manufacturing processes, mechanical properties and precipitations for aluminum lithium alloys used in aeronautic applications. *Heliyon* **2023**, *9*, e12565. [[CrossRef](#)]
23. Wanhill, R.J.H.; Bray, G.H. *Chapter 12—Fatigue Crack Growth Behavior of Aluminum–Lithium Alloys*; Eswara Prasad, N., Gokhale, A.A., Wanhill, R.J.H., Eds.; Butterworth-Heinemann: Boston, UK, 2014; pp. 381–413. [[CrossRef](#)]
24. Srivatsan, T.S.; Lavernia, E.J.; Eswara Prasad, N.; Kutumbarao, V.V. *Chapter 10—Quasi-Static Strength, Deformation, and Fracture Behavior of Aluminum–Lithium Alloys*; Eswara Prasad, A.N., Gokhale, A., Wanhill, R.J.H., Eds.; Butterworth-Heinemann: Boston, UK, 2014; pp. 305–339. [[CrossRef](#)]
25. Semenov, A.M.; Sinyavskiy, V.; Kalinin, V.D. Corrosion resistance of aluminum-lithium alloys under various climatic conditions. *Prot. Met. Phys. Chem. Surfaces* **2014**, *50*, 236–243. [[CrossRef](#)]
26. Liu, D.; Wang, J.; Li, J. Microstructures evolution and mechanical properties disparity in 2070 Al-Li alloy with minor Sc addition. *Trans. Nonferrous Met. Soc. China* **2018**, *28*, 2151–2161. [[CrossRef](#)]
27. Staroselsky, A.; Borkowski, L. Microstructural Characterization and Simulation of High Temperature Inelastic Deformation and Fracture of Al-Li 2070. *J. Mater. Eng. Perform.* **2019**, *28*, 6942–6957. [[CrossRef](#)]
28. Lumley, R.N.; Schaffer, G.B. The effect of solubility and particle size on liquid phase sintering. *Scr. Mater.* **1996**, *35*, 589–595. [[CrossRef](#)]
29. Schaffer, G.B.; Sercombe, T.B.; Lumley, R.N. Liquid phase sintering of aluminum alloys. *Mater. Chem. Phys.* **2001**, *67*, 85–91. [[CrossRef](#)]
30. ASTM B311-17; Standard Test Method for Density of Powder Metallurgy (PM) Materials Containing Less Than Two Percent Porosity. ASTM International: West Conshohocken, PA, USA, 2017.
31. UNE EN ISO 3325; Sintered Metal Materials, Excluding Hardmetals—Determination of Transverse Rupture Strength. ISO: Geneva, Switzerland, 2002.
32. Belov, N.A.; Eskin, D.G.; Aksenov, A.A. *Chapter 5—Alloys of the Al–Cu–Mn–(Mg, Fe, Si) System*; Belov, N.A., Eskin, D.G., Aksenov, A.A., Eds.; Elsevier: Oxford, UK, 2005; pp. 159–192. [[CrossRef](#)]
33. Jiao, S.; Cheng, X.; Shen, S.; Wang, X.; He, B.; Liu, D.; Wang, H. Microstructure evolution and mechanical behavior of Al-Li alloy fabricated by laser melting deposition technique. *J. Alloys Compd.* **2020**, *821*, 153125. [[CrossRef](#)]
34. McPhee, W.A.G.; Schaffer, G.B.; Drennan, J. The effect of iron on liquid film migration and sintering of an Al–Cu–Mg alloy. *Acta Mater.* **2003**, *51*, 3701–3712. [[CrossRef](#)]

35. Reddy, M.P.; Manakari, V.; Parande, G.; Shakoor, R.A.; Mohamed AM, A.; Gupta, M. Structural, mechanical and thermal characteristics of Al-Cu-Li particle reinforced Al-matrix composites synthesized by microwave sintering and hot extrusion. *Compos. Part. B Eng.* **2019**, *164*, 485–492. [[CrossRef](#)]
36. Partridge, P.G. Oxidation of aluminium-lithium alloys in the solid and liquid states. *Int. Mater. Rev.* **1990**, *35*, 37–58. [[CrossRef](#)]
37. Qi, M.; Chen, C.; Wei, J.; Mei, X.; Sun, C.; Su, G.; Zhang, C.; Yan, M.; Yang, F.; Guo, Z. Superior mechanical properties and microstructural evolution of powder metallurgy 2195 Al-Li alloy subjected to hot extrusion. *J. Alloys Compd.* **2023**, *962*, 171184. [[CrossRef](#)]
38. Rodríguez-González, P.; Ruiz-Navas, E.M.; Gordo, E. Effect of Heat Treatment Prior to Direct Hot-Extrusion Processing of Al-Cu-Li Alloy. *Metals* **2022**, *12*, 1046. [[CrossRef](#)]
39. Zhang, D.; Zou, H.; Cai, S. Effect of Iron Coating on Thermal Properties of Aluminum-Lithium Alloy Powder. *Propellants Explos. Pyrotech.* **2017**, *42*, 953–959. [[CrossRef](#)]
40. Mishra, R.S.; Sidhar, H. *Chapter 2—Physical Metallurgy of 2XXX Aluminum Alloys*; Mishra, R.S., Sidhar, H., Eds.; Butterworth-Heinemann: Boston, UK, 2017; pp. 15–36. [[CrossRef](#)]
41. Madhusudhan Reddy, G.; Gokhale, A.A. *Chapter 9—Welding Aspects of Aluminum–Lithium Alloys*; Prasad, N.E., Gokhale, A.A., Wanhill, R.J.H., Eds.; Butterworth-Heinemann: Boston, UK, 2014; pp. 259–302. [[CrossRef](#)]
42. Xun, C.; Li, X.; Wen, K.; Zhu, K.; Gao, G.; Li, Z.; Zhang, Y.; Xiong, B. Influence of enhanced Li content on the as-cast eutectic phase features and the evolution during homogenization of Al-Cu-Li alloys. *J. Mater. Res. Technol.* **2023**, *26*, 8555–8568. [[CrossRef](#)]
43. Tsubakino, H.; Nozato, R.; Sakurai, T.; Hasegawa, Y.; Hayashi, Y. Precipitation of metastable δ' in Al-1.9Li-2.5Mg alloy. *Mater. Sci. Technol.* **1994**, *10*, 222–226. [[CrossRef](#)]
44. Bo, L.; Xiangxiang, H.; Rui, X.; Yuliang, Z.; Yemao, L.; Huaqiang, X. Evolution of iron-rich intermetallics and its effect on the mechanical properties of Al-Cu-Mn-Fe-Si alloys after thermal exposure and high-temperature tensile testing. *J. Mater. Res. Technol.* **2023**, *23*, 2527–2541. [[CrossRef](#)]
45. Madhankumar, S.; Sivakumar, K.; Chandradass, J.; Addanki, R.S.; Rodriguez, V.A.; Saroshkumar, U. Enhancement of mechanical properties and tribological properties of aluminum using Iron(Fe) and Nickel(Ni) additives. *Mater. Today Proc.* **2021**, *45*, 6852–6856. [[CrossRef](#)]
46. Novák, P.; Benediktová, D.; Mestek, S.; Tsepeleva, A.; Kopeček, J. Aluminum alloys with natural ratio of alloying elements manufactured by powder metallurgy. *J. Alloys Compd.* **2023**, *931*, 167440. [[CrossRef](#)]
47. Navas EM, R.; Palenzuela, B.R. Sintering of Aluminum Alloys. Processing and Properties. *Encycl. Mater. Met. Alloys* **2022**, *3*, 343–352.

Disclaimer/Publisher’s Note: The statements, opinions and data contained in all publications are solely those of the individual author(s) and contributor(s) and not of MDPI and/or the editor(s). MDPI and/or the editor(s) disclaim responsibility for any injury to people or property resulting from any ideas, methods, instructions or products referred to in the content.